Automated Fluorescence and Reflectance Coregistered 3-D Tissue Imaging System

Zhaolong Shen, Alek Nacev, Azeem Sarwar, Roger Lee, Didier Depireux, and Benjamin Shapiro

Fischell Department of Bioengineering, University of Maryland, College Park, MD 20742 USA
The Institute for Systems Research, University of Maryland, College Park, MD 20742 USA

An automated system was developed to image the 3-D distribution of fluorescent magnetic nanoparticles in tissue samples. It enables easy measurement of magnetic nanoparticle distributions, for small and large tissue samples (currently up to a maximum size of 25 mm × 25 mm × 25 mm), in 3-D, with about 70 μm resolution in plane and 1 μm in the vertical direction. There is a linear correlation between particle concentration and fluorescence intensity, hence the system provides a quantitative measure of the nanoparticle distribution, but the tissue sample is destroyed during the imaging process. The system was demonstrated by measuring the particle distribution in rat ear and brain samples.

Index Terms—Cryostat, drug targeting, fluorescence imaging, histology, image registration, magnetic nanoparticles, reflectance imaging, tissue imaging.

I. INTRODUCTION

IRON oxide magnetic nanoparticles are of interest to researchers due to their promising biomedical applications [1]–[4]. Among these is magnetic drug targeting, a process in which drug loaded magnetic nanoparticles are injected either intravenously [5] or through an artery [6], and guided through biological tissues to a diseased site by magnetic fields [7]. The advantage of using iron oxide magnetic nanoparticles is that they are biocompatible [8] and can be multifunctionalized with different coating, fluorescent labeling, drug, and other active coupling compounds [9], [10].

To evaluate the effectiveness of magnetic targeting, it is desirable to know the distribution of particles in tissue, and to evaluate such distributions against tissue morphology. Such data can provide information on how the nanoparticles have traveled through tissue, how they have progressed through vessels versus different types of tissue, and where ultimately they reside. In Table I, a list of existing techniques for imaging nanoparticles' 3 dimensional (3-D) distribution in biological tissue is summarized. Both X-ray computed tomography (CT) and magnetic resonance imaging (MRI) are able to provide anatomical imaging and the nanoparticles' spatial distribution simultaneously [11], [12]. However their spatial resolution and detection limits are too low to resolve fine histological structures or the distribution of low concentrations of nanoparticles [13], [14]. Magnetic particle imaging (MPI) can only image the magnetic nanoparticles' themselves but has a higher sensitivity than CT and MRI [15]. Nanoparticles labeled with radionuclides can be imaged by positron emission tomography (PET) [16] and single photon emission computation tomography (SPECT) [17]. In [18], [19], a new method called magnetomotive optical coherence tomography (MM-OCT) was proposed to image magnetically labeled

TABLE I
SUMMARY OF 3-D NANOPARTICLE IMAGING TECHNIQUES

Methods	Labels	Signal Detected	Cost	Range (particles / mL)	References
CT	none	x-rays	medium	$10^{17} \sim 10^{20}$	[29], [30]
MRI	none	magnetic-fields	high	$10^{16} \sim 10^{20}$	[14], [31]–[33]
MPI	magnetic	magnectic-fields	high	$10^{15} \sim 10^{20}$	[15], [34], [35]
PET	radionuclide	positrons	high	$10^{14} \lesssim$	[34], [36]
SPECT	radionuclide	γ-rays	high	$10^{15} \sim 10^{20}$	[37], [38]
FMT	NIR emitter	light	medium	$10^{14} \sim 10^{15}$	[28], [36], [39], [40]
MM-OCT	magnetic	light	medium	$10^{17} \lesssim$	[18], [19]
Cryostat	fluorescent	light	low	$10^{9} \lesssim$	

cells in three dimensions by adding a modulated magnetic field to a traditional OCT. There are some other imaging modalities including episcopic 3-D imaging [20], episcopic fluorescence image capturing (EFIC) [21], high resolution episcopic microscopy (HREM) [22], surface imaging microscopy (SIM) [23], [24] and 3-D cryo-imaging [25], that are based on tissue slicing and surface imaging to generate high resolution 3-D images of the sample. They all have their own advantages and disadvantages.

Our imaging technique is based on fluorescence reporting of nanoparticles. Fluorescent reporter technologies have been used widely for tagging or labeling of biological molecules and cells [26]. Hence a number of fluorescence imaging techniques has been developed to visualize and quantify fluorescent markers [27], [28]. For example, the fluorescence-mediated tomography (FMT) can be used to image nanoparticles labeled with near infrared emitters in tissue [28]. However, the imaging depth of these techniques is generally limited due to the limited penetration depth of light.

Here, we extend fluorescence reporting to deep tissue by using a cryostat linked to an automated optical imaging system. The key idea is simple: we image the top of the sample, then cut away a thin slice using the cryostat, then image the next slice, and we repeat this process to create a 3-D image of the entire sample. Our optical system has both laser-induced fluorescence imaging and reflectance imaging. For the fluorescence signals, the magnetic nanoparticles are coated with fluorescent dyes and are excited by a homogenized laser illumination. For the reflectance signals, two light emitting diodes (LEDs) are used

to illuminate the top of the sample. Two cameras are synchronized to take both fluorescence and reflectance images of each slice. The two images are registered with each other and a sequence of these images is used to reconstruct a 3-D model of the histology of the sample and the nanoparticles distribution inside it.

The spatial resolution of the system (see Fig. 3) was determined by imaging a standard U.S. Air Force (USAF) test target (USAF 1951 HI-RES, Edmund Optics Inc.), which is made by patterning the 1951 USAF resolution test chart on a glass. The relationship between fluorescence intensity and nanoparticle concentration was calibrated by imaging a sequence of gelatin samples with different nanoparticles concentrations (see Fig. 4). Finally, biological samples including rat ear and brain were imaged (see Figs. 5 and 6). Our system enables easy measurement of magnetic nanoparticle distributions, for small and large tissue samples (currently up to a maximum size of $25 \text{ mm} \times 25 \text{ mm} \times 25 \text{ mm}$) in 3 dimensions, with 70 μm resolution in plane and 1 μm in the vertical direction. The detection limit is 1×10^9 particles per milliliter (mL), which compares favorably with $10^{17}/\text{mL}$, $10^{16}/\text{mL}$, $10^{15}/\text{mL}$, $10^{15}/\text{mL}$, $10^{14}/\text{mL}$ respectively for CT, MRI, MPI, PET, SPECT, and FMT (see Table I). The main drawback of our system is that the sample is destroyed by the cryostat slicing, although the method can be paused to save single histology slices for later use.

II. METHODS

Our imaging system is composed of three subsystems: a cryostat, an optical imaging system, and an automated control system. The cryostat is modified and used to slice the tissue sample continuously. The control system synchronizes the illumination and imaging of the optical imaging system with the slicing action of the cryostat. The fluorescence and reflectance cameras share the same imaging optics and their sensor sizes are chosen to be identical, allowing for the images taken by the two cameras to be coregistered. After slicing, the planar image stacks are post-processed to generate the 3-D model.

A. Cryostat System

A cryostat is usually used to cut off thin slices from a tissue block for subsequent histology analysis [41]. Here the cryostat (5030 microtome, Bright) was used as shown in Fig. 1(c). The tissue sample was prepared by embedding it in optimal cutting temperature compound (OCT) prior to being frozen. The frozen tissue sample was then placed on top of the tissue holder of the cryostat. The cryostat can be operated in two modes: manual and motorized. We used the motorized mode, which is activated by engaging a bolt on the wheel disk. For each rotation of the wheel disk, the tissue holder moves up a specific distance (the slicing thickness, ranging from 1 to 30 μm). Then the sample moves horizontally underneath the cryostat blade to cut off one slice. This process repeats. Once the tissue holder reaches its maximum vertical displacement of 4 mm, it has to be rewound to allow another sample to be sliced. Hence the 5030 microtome can continuously slice tissues for a maximum height of 4 mm. During cutting, the chamber temperature of the cryostat is kept
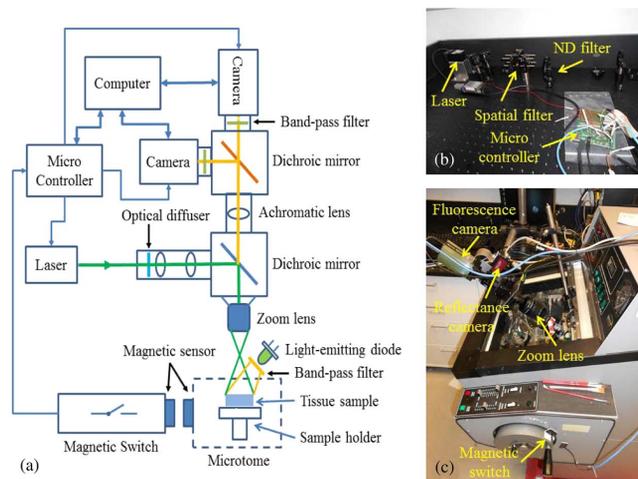
Fig. 1. Cryostat imaging system. (a) Schematic of the automated fluorescence and reflectance coregistered 3-D tissue imaging system. (b) A 532 nm green laser is used as an excitation source and a micro-controller is programmed to control the imaging process. (c) A cryostat is used to remove slices from the top of the tissue sample, which is illuminated simultaneously by the laser and two LEDs. Two cameras are synchronized to take both fluorescence and reflectance images after each slice.

at a user specified value (typically around $-20 \, ^\circ$C) to keep the sample frozen during slicing.

The cryostat was customized by the addition of a magnetic switch on the wheel disk for synchronizing the slicing, illuminating, and imaging of the tissue sample. The moving component of the magnetic switch was attached to the edge of the wheel disk while the stationary component was fixed to the body of the cryostat. Each time the moving component passes by the stationary component, the magnetic switch activates and signals the control system to initiate another round of image acquisition.

B. Optical Imaging System

The optical imaging system is designed to illuminate and image the tissue sample in both fluorescence and reflectance channels. It is composed of two illumination sources, one zoom lens, one relay lens, and two cameras for fluorescence and reflectance imaging respectively. Since the two cameras share the same optical imaging path, the two images can be easily aligned and coregistered with each other. The fluorescent magnetic nanoparticles used in this research is nano-screenMAG/R-D (Chemicell, Germany), which has a core-shell structure. It consists of a magnetite core covered by fluorescence dye for fluorescence detection. A second layer envelops the particle with starch matrix which protects the particles against aggregation. The peak excitation wavelength of the particle is 578 nm and the peak emission wavelength is 613 nm.

Two illumination sources were used for laser-induced fluorescence imaging and reflectance imaging respectively. A transistor-to-transistor level (TTL) modulated green laser (PGLVH532, Information Unlimited, wavelength 532 nm, power 150 mW), was used to excite fluorescence signal from the fluorescent magnetic nanoparticles. The laser beam is first collimated and expanded, and then diverted into an optical diffuser (ED1-S20-MD, Thorlabs) for a homogenized intensity distribution. Two condensing lenses were placed after the
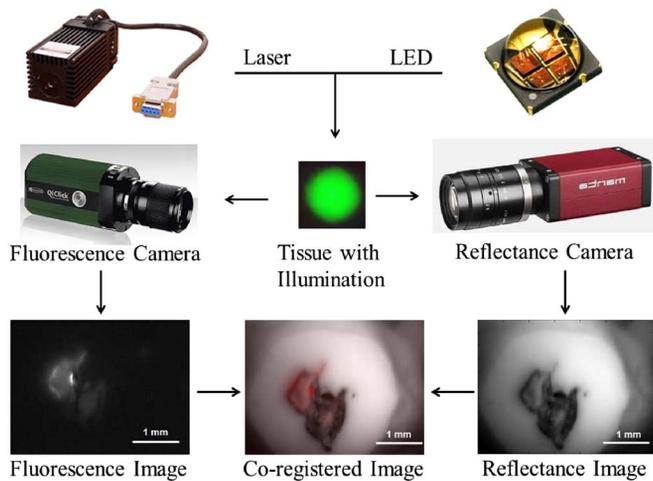
Fig. 2. Schematic of the coregistered fluorescence and reflectance imaging process. Two illumination sources, a laser and LEDs, are directed onto the top of the tissue sample. The resulting fluorescence and reflectance signals are separated and collected by two cameras: a fluorescence camera and a reflectance camera respectively. The fluorescence and reflectance images of each tissue slice are combined for coregistered imaging.

optical diffuser to compensate for the divergence of the beam. The homogenized laser beam was reflected by a dichroic mirror (MD568, Thorlabs) and illuminated the top of the tissue sample after passing through a zoom lens (EFS18-55 mm, Canon). The illumination source for the reflectance imaging is composed of two LEDs. Two high power green LED emitters (LZ4-00G110, LedEngin Inc., power 10 W) were mounted inside the chamber of the cryostat to illuminate the top of the tissue sample for reflectance imaging. To eliminate the interference with the fluorescence imaging, a band-pass filter (MF565-24, Thorlabs) was placed in front of each LED. The excited fluorescence signals and reflectance signals from the top of the tissue sample were imaged using two cameras, and then registered to create a combined fluorescence and reflectance image. The fluorescence signal excited by the laser and the reflectance signal from the LED light were both collected by the zoom lens. An achromatic doublet lens (AC254-040-A, Thorlabs) was used as a relay lens to relay the image onto the sensors of the two cameras. After separation by a dichroic mirror (MF620-52, Thorlabs), the fluorescence signal was imaged onto the fluorescence camera (QIClick, Qimaging) after passing through an emission filter (MF620-52, Thorlabs). The reflectance signal was also separated by the dichroic mirror and imaged onto the reflectance camera (Manta G-145, Allied Vision) after passing through another emission filter (MF565-24, Thorlabs). Since the two cameras shared the same imaging optics and their sensor sizes were chosen to be identical, the images taken by the two cameras were readily coregistered. This imaging process is illustrated in Fig. 2.

C. Automated Control System

A control system was built to automate the imaging process. A micro-controller board (ADuC7026, ADI) is notified by the magnetic switch, and initiates the illuminating laser and the two cameras by sending TTL signals to each of them through its digital I/O pins. The laser is pulsed to excite the fluorescence

signal from the top of the tissue sample, which is within the focal plane of the cameras. The two cameras are also triggered by the micro-controller. This imaging process can be paused or restarted at any time—e.g., to remove and save a histology slice for later use.

A graphical user interface program (GUI) was developed in Matlab (Mathworks) for user interaction, real-time image display and data logging. The GUI was notified by the micro-controller through the serial port to display and save the acquired images in real time. All the imaging parameters including exposure time, gain, slice thickness and slice numbers are recorded for the subsequent image processing.

D. System Calibration and Sample Preparation

The system was first calibrated, for spatial resolution and fluorescence intensity, in two dimensions. The spatial resolution of the system was measured by imaging a standard USAF resolution test target. The USAF resolution test target was imaged by the fluorescence camera but with white light illumination.

The relationship between the fluorescence intensity and the concentration of nanoparticles was calibrated by imaging a sequence of samples containing nanoparticles suspended in gelatin at different dilutions. A gelatin-water solution was first prepared by adding 2 g of gelatin powder to 100 mL of deionized water and heating the solution for 2 min. Then the calibration samples were prepared by diluting fluorescent magnetic nano-screenMAG/R-D nanoparticles (particle size 200 nm, stock concentration of $1.3 \times 10^{12}/\text{mL}$ from Chemicell) into the gelatin-water solution. The dilution ratio ranged from 1:10 to 1:5120 with ten different dilutions. Each dilution was mixed and sonicated for 10 min before 200 μL of the dilution was placed into a circular plastic cap with an inner diameter of 10 mm. The cap was brought into the chamber of the cryostat to solidify the gelatin and then imaged by the fluorescence camera with both laser and LED illuminations. The exposure time of the fluorescence camera was set to be 0.1 s while the gain of the camera was varied for different dilutions. Ten images were captured for each sample and averaged for calculating the fluorescence intensity. A square window centered on the sample was defined in the image with window size 450 $\times$ 450 pixels. The camera gains were changed from sample to sample to acquire images without saturation. To compare intensity calibrations between samples, the pixel intensity within the window was divided by the camera gain for each sample. Then the net fluorescence intensity of the sample was determined by calculating the average pixel value over the window image.

For tissue imaging, Long Evans rats (obtained from vendor Charles River) were used for this study. All surgical and experimental procedures were approved by the University of Maryland Animal Care and Use Committee and were in accord with NIH Guidelines on the care and use of laboratory animals. Rats were sacrificed and their organs including ears and brains were excised for imaging to demonstrate both the 2-D and 3-D imaging capability of the system. For 2-D imaging, the rats were first anesthetized with Isoflurane gas delivered by a face mask. 40 μL of fluid containing about 3.3×10^{12} of 300 nm diameter starch coated red fluorescent magnetic particles (nano-screen MAG/R-D, Chemicell), was injected
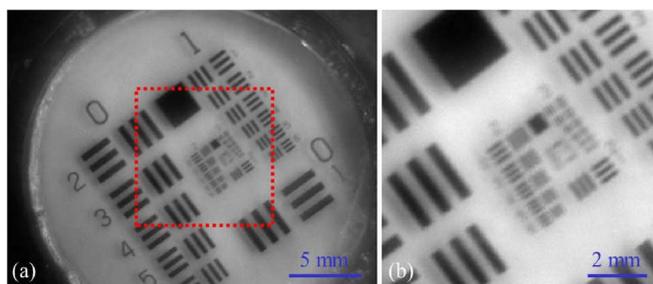
Fig. 3. Optical resolution calibration. (a) Wide-field image of the USAF target. (b) Enlarged image showing the red dot rectangle area in the original image. The minimum discernable bar is group 2 level 6, which corresponds to an optical resolution of 70 μm.

into the external ear (into the ear canal) over the tympanic membrane. An assembly of four NdFeB Grade N42 magnets was employed to pull particles into the middle ear of rats. The rat was subjected to magnetic pull for 2 h and was euthanized immediately thereafter in a carbon dioxide chamber. After euthanasia, the rat ear including ear canal, eardrum and part of the middle ear was removed for imaging.

Rat brains were extracted right after the euthanasia of the rats in a carbon dioxide chamber and then stored in phosphate buffered saline at 37 °C for further use. A volume of 20 μL fluorescent magnetic nanoparticle solution (particle size 100 nm, nano-screenMAG/R-D, Chemicell) was injected into the brain from the spinal cord side. A magnet ($1 \times 1 \times 2$ inch, 1.42 T remnant magnetization) was placed on the other side for 1.5 h to pull the magnetic particles to the other end of the brain. The brain was flash frozen in liquid nitrogen after the magnetic pull experiment. The sample was then prepared by immersing the brain into a liquid OCT column. This column sample was stored at -20 °C for at least another 30 min before slicing in the cryostat. The acquired fluorescence and reflectance image stacks were first preprocessed by a Matlab script to registered with each other. Then these image stacks were loaded into a free, open source visualization software (3DSlicer) for registration, segmentation, quantification, filtering and 3-D model reconstruction.

III. RESULTS AND DISCUSSION

A. Spatial Resolution Calibration

As shown in Fig. 3(a), the USAF target was imaged with a field of view of 25 mm × 25 mm. An enlarged view of the red dot rectangle area is shown in Fig. 3(b). The in-plane optical resolution of the system was determined to be 70 μm. This in-plane optical resolution can be further increased by using a relay lens with higher numerical aperture.

B. Fluorescence Intensity Calibration

The window images are shown in Fig. 4(a) labeled with their corresponding dilution ratio. The net fluorescence intensity versus the inverse of the dilution ratio is shown Fig. 4(b). Since the inverse of the dilution is proportional to nanoparticle concentration, in Fig. 4(b) the net fluorescence intensity is graphed versus the inverse of the dilution ratio. The fluorescent
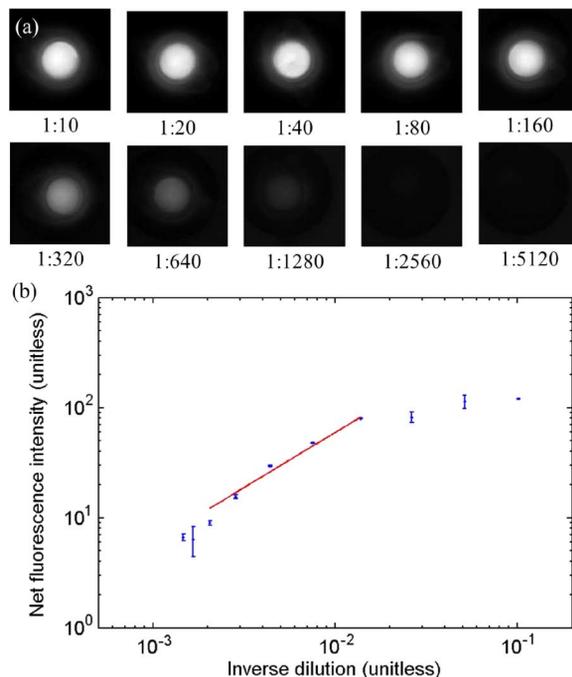
Fig. 4. Fluorescence intensity calibration. (a) Fluorescence images of a sequence of samples with different dilution ratio. (b) Fluorescence intensity and error bar versus the inverse of dilution ratio. The red line is the fitting line to the data points in linear region.

intensity of the image was linearly correlated with the nanoparticle concentration in the region of $1280 \leq$ dilution ≤ 80, which was the observed linear range. For the two samples with highest dilution ratio, the fluorescence signals of these samples were too weak to be detected, which determined the detection limit of the system. This detection limit can be reduced by increasing the exposure time. For the three samples where the dilution ratio was below 40, the nanoparticle concentration was sufficiently high to saturate the imaging. Note that this saturation can be readily eliminated by choosing a lower gain or exposure time for the camera. The 1:1280 dilution detection limit corresponded to a nanoparticle concentration of 1×10^9 particles/mL. By fitting the linear region of the data [see Fig. 4(b)], we found that the relationship between the fluorescence intensity and the concentration can be characterized by the following equation:

$$I = 4.57 \times 10^{-9} \times C + 7.6 \tag{1}$$

where I is the fluorescence intensity and C is the concentration of nanoparticles with units mL^{-1} (with $R^2 = 0.9986$). This fitting line is also shown in Fig. 4(b). Note that a coordinates transformation

$$C = C + 0.0013 \tag{2}$$

is used to make sure that the fitting line is a straight line in the plot where x- and y-axes are on a logarithmic scales.

C. Co-Registered Tissue Imaging

1) 2-D Coregistered Imaging of Rat Ear: Fig. 5(b) shows the fluorescence image of a slice through the middle of the
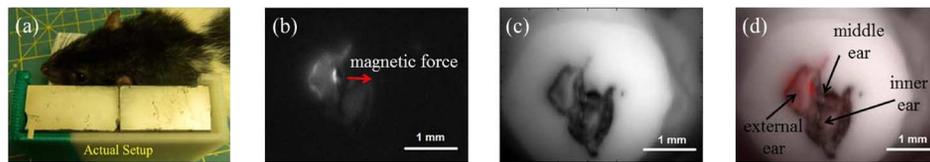
Fig. 5. Coregistered 2-D imaging of a rat ear. (a) Experimental setup for magnetic pull from external ear into middle ear. (b) Fluorescent image of a slice through the middle of the ear. (c) and (d) Reflectance and coregistered image of the same slice.
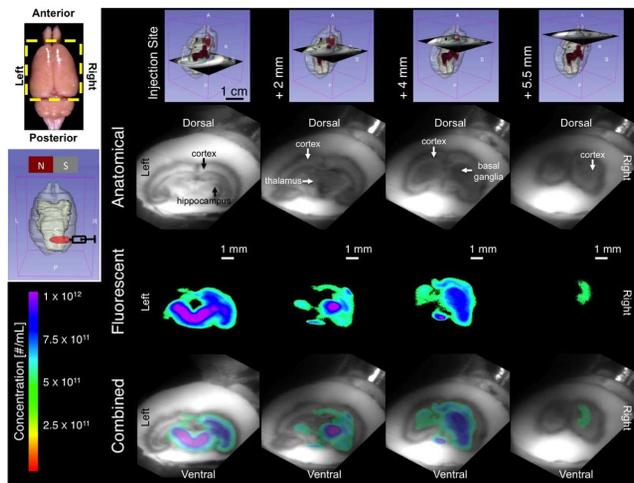
Fig. 6. Coregistered 2- and 3-D image of a rat brain reconstructed in 3DSlicer software. The fluorescent magnetic nanoparticle concentration values are determined from the calibrated fluorescence intensity curve.

ear. The fluorescence intensity distribution represents the concentration distribution of the fluorescent magnetic nanoparticles in that slice. By registering with the reflectance image in Fig. 5(c), the coregistered image is generated in Fig. 5(d). Note that the relative position shift of the tissue within the fluorescence and reflectance images is due to the misalignment of the dichroic mirror. It can be readily corrected by adjusting the orientation angle of the mirror. The nonuniform illumination in the reflectance image can also be corrected by adjusting the illumination angle of the LEDs.

2) 3-D Coregistered Imaging of Rat Brain: Fig. 6 shows the coregistered 3-D image of the rat brain reconstructed in 3DSlicer. The fluorescence signals are shown in red and are registered with the morphological structure of the brain in all three dimensions. Four sample reflectance images of the brain slices are shown to illustrate the anatomical structure of the rat brain at different depths, including cortex, hippocampus, thalamus, and basal ganglia. The corresponding fluorescence images and the combined coregistered images are also presented to show the concentration distribution of the delivered fluorescent magnetic nanoparticles. The concentration values are determined from the calibrated (1). A coregistered 3-D orthogonal image of the brain is reconstructed to show the anatomical 3-D structure of the brain and the magnetic nanoparticles distribution in this structure.

IV. CONCLUSION

An automated optical imaging system was developed to image biological tissue samples in three dimensions with coregistered fluorescence and reflectance imaging capability. The experimental results indicated that the system enables measurement of fluorescent nanoparticle distributions in biological tissues with a tissue block size up to $25\,\text{mm} \times 25\,\text{mm} \times 25\,\text{mm}$. The fluorescent nanoparticle concentration can also be determined from the fluorescence intensity versus concentration curve. The spatial resolution of the system in all three axes was on the order of microns, which is superior to other imaging modalities, such as conventional CT and MRI, whose spatial resolution are usually on the order of millimeters. The optical resolution of the system can be further improved by using a relay lens with a higher numerical aperture. The optical resolution and imaging area can also be increased by employing digital stitching technique [42] at the expense of higher system complexity and lower imaging speed.

REFERENCES

[1] T. Yoshino, H. Hirabe, M. Takahashi, M. Kuhara, H. Takeyama, and T. Matsunaga, "Magnetic cell separation using nano-sized bacterial magnetic particles with reconstructed magnetosome membrane," *Biotechnol. Bioeng.*, vol. 101, no. 3, pp. 470–477, 2008.

[2] C. Sun, J. S. Lee, and M. Zhang, "Magnetic nanoparticles in MR imaging and drug delivery," *Adv. Drug Del. Rev.*, vol. 60, no. 11, pp. 1252–1265, 2008.

[3] M. Mahmoudi, S. Sant, B. Wang, S. Laurent, and T. Sen, "Superparamagnetic iron oxide nanoparticles (SPIONs): Development, surface modification and applications in chemotherapy," *Adv. Drug Del. Rev.*, vol. 63, no. 1–2, pp. 24–46, 2011.

[4] S. Lee, M. Muthiah, H. Lee, H.-J. Lee, M.-J. Moon, H.-L. Che, S. Heo, H.-C. Lee, Y. Jeong, and I.-K. Park, "Synthesis and characterization of magnetic nanoparticle-embedded multi-functional polymeric micelles for MRI-guided gene delivery," *Macromolecular Res.*, vol. 20, pp. 188–196, 2012.

[5] P. Oswald, O. Clement, C. Chambon, E. Schouman-Claeys, and G. Frija, "Liver positive enhancement after injection of superparamagnetic nanoparticles: Respective role of circulating and uptaken particles," *Magn. Resonance Imaging*, vol. 15, pp. 1025–1031, 1997.

[6] H. Ma, X. Qi, W. Ding, Y. Maitani, and T. Nagai, "Magnetic targeting after femoral artery administration and biocompatibility assessment of superparamagnetic iron oxide nanoparticles," *J. Biomed. Mater. Res. A*, vol. 84, pp. 598–606, 2008.

[7] T. Xanthos, M. Chatzigeorgiou, E. O. Johnson, and A. Chalkias, "Magnetically targeted drug delivery during cardiopulmonary resuscitation and the post-resuscitation period," *Resuscitation*, vol. 83, no. 7, pp. 803–805, 2012.

[8] R. K. Singh, T.-H. Kim, K. D. Patel, J. C. Knowles, and H.-W. Kim, "Biocompatible magnetite nanoparticles with varying silica-coating layer for use in biomedicine: Physicochemical and magnetic properties, and cellular compatibility," *J. Biomed. Mater. Res. Part A*, vol. 100A, no. 7, pp. 1734–1742, 2012.

[9] N. Chekina, D. Horak, P. Jendelova, M. Trchova, M. J. Benes, M. Hruby, V. Herynek, K. Turnovcova, and E. Sykova, "Fluorescent magnetic nanoparticles for biomedical applications," *J. Mater. Chem.*, vol. 21, pp. 7630–7639, 2011.

[10] J. Xie, G. Liu, H. S. Eden, H. Ai, and X. Chen, "Surface-engineered magnetic nanoparticle platforms for cancer imaging and therapy," *Accounts Chem. Res.*, vol. 44, no. 10, pp. 883–892, 2011.

[11] A. M. Rad, A. S. Arbab, A. S. M. Iskander, Q. Jiang, and H. Soltanian-Zadeh, "Quantification of superparamagnetic iron oxide (spio)-labeled cells using MRI," *J. Magn. Resonance Imaging*, vol. 26, no. 2, pp. 366–374, 2007.

[12] T. Johnson, C. Fink, S. Schnberg, and M. Reiser, *Dual Energy CT in Clinical Practice*, ser. Medical Radiology. Berlin, Germany: Springer-Verlag, 2011.

[13] H. Pardoe, W. Chua-anusorn, T. Pierre, and J. Dobson, "Detection limits for ferrimagnetic particle concentrations using magnetic resonance imaging based proton transverse relaxation rate measurements," *Phys. Med. Biol.*, vol. 48, no. 6, p. N89, 2003.

[14] H. Dahnke and T. Schaeffter, "Limits of detection of spio at 3.0 t using t2 ∗ relaxometry," *Magn. Resonance Med.*, vol. 53, no. 5, pp. 1202–1206, 2005.

[15] J. Weizenecker, B. Gleich, J. Rahmer, H. Dahnke, and J. Borgert, "Three-dimensional real-time in vivo magnetic particle imaging," *Phys. Med. Biol.*, vol. 54, no. 5, pp. 48–57, 2009.

[16] M. Ogawa, S. Ishino, T. Mukai, D. Asano, N. Teramoto, H. Watabe, N. Kudomi, M. Shiomi, Y. Magata, H. Iida, and H. Saji, "(18)f-fdg accumulation in atherosclerotic plaques: Immunohistochemical and PET imaging study," *J. Nuclear Med.*, vol. 45, no. 7, pp. 1245–1250, 2004.

[17] M. T. Madsen, "Recent advances in SPECT imaging," *J Nuclear Med.*, vol. 48, no. 4, pp. 661–673, 2007.

[18] A. Oldenburg, F. Toublan, K. Suslick, A. Wei, and S. Boppart, "Magnetomotive contrast for in vivo optical coherence tomography," *Opt. Exp.*, vol. 13, no. 17, pp. 6597–6614, 2005.

[19] A. Oldenburg, J. Gunther, and S. Boppart, "Imaging magnetically labeled cells with magnetomotive optical coherence tomography," *Opt. Exp.*, vol. 30, no. 7, pp. 747–749, 2005.

[20] W. J. Weninger and S. H. Geyer, "Episcopic 3d imaging methods: Tools for researching gene function," *Curr. Genomics*, vol. 9, no. 4, pp. 282–289, 2008.

[21] W. J. Weninger and T. Mohun, "Phenotyping transgenic embryos: A rapid 3-d screening method based on episcopic fluorescence image capturing," *Nat. Genet.*, vol. 30, no. 1, pp. 59–65, 2002.

[22] W. Weninger, S. Geyer, T. Mohun, D. Rasskin-Gutman, T. Matsui, I. Ribeiro, L. Costa, J. Izpisa-Belmonte, and G. Mller, "High-resolution episcopic microscopy: A rapid technique for high detailed 3d analysis of gene activity in the context of tissue architecture and morphology," *Anatomy Embryol.*, vol. 211, no. 3, pp. 213–221, 2006.

[23] A. J. Ewald, H. Mcbride, M. Reddington, S. E. Fraser, and R. Kerschmann, "Surface imaging microscopy, an automated method for visualizing whole embryo samples in three dimensions at high resolution," *Develop. Dyn.*, vol. 225, no. 3, pp. 369–375, 2002.

[24] D. A. Gerneke, G. B. Sands, R. Ganesalingam, P. Joshi, B. J. Caldwell, B. H. Smaill, and I. J. Legrice, "Surface imaging microscopy using an ultramiller for large volume 3d reconstruction of wax- and resin-embedded tissues," *Microscopy Res. Techn.*, vol. 70, no. 10, pp. 886–894, 2007.

[25] D. Roy, G. J. Steyer, M. Gargesha, M. E. Stone, and D. L. Wilson, "3d cryo-imaging: A very high-resolution view of the whole mouse," *Anatomical Record: Adv. Integr. Anatomy Evol. Biol.*, vol. 292, no. 3, pp. 342–351, 2009.

[26] M. Bruchez, M. Moronne, P. Gin, S. Weiss, and A. P. Alivisatos, "Semiconductor nanocrystals as fluorescent biological labels," *Science*, vol. 281, no. 5385, pp. 2013–2016, 1998.

[27] H. Nasir, "Fluorometric method for the simultaneous quantitation of differently-sized nanoparticles in rodent tissue," *Int. J. Pharm.*, vol. 214, pp. 55–61, 2001.

[28] X. Montet, V. Ntziachristos, J. Grimm, and R. Weissleder, "Tomographic fluorescence mapping of tumor targets," *Cancer Res.*, vol. 65, no. 14, pp. 6330–6336, 2005.

[29] H. Elleaume, A. M. Charvet, S. Corde, F. Esteve, and J. F. Le Bas, "Performance of computed tomography for contrast agent concentration measurements with monochromatic x-ray beams: Comparison of k-edge versus temporal subtraction," *Phys. Med. Biol.*, vol. 47, no. 18, pp. 3369–3385, 2002.

[30] J. L. Ducote, Y. Alivov, and S. Molloi, "Imaging of nanoparticles with dual-energy computed tomography," *Phys. Med. Biol.*, vol. 56, no. 7, pp. 2031–2044, 2011.

[31] M. Nahrendorf, H. Zhang, S. Hembrador, P. Panizzi, D. E. Sosnovik, E. Aikawa, P. Libby, F. K. Swirski, and R. Weissleder, "Nanoparticle PET-CT imaging of macrophages in inflammatory atherosclerosis," *Circulation*, vol. 117, no. 3, pp. 379–387, 2008.

[32] J. C. Wood, C. Enriquez, N. Ghugre, J. M. Tyzka, S. Carson, M. D. Nelson, and T. D. Coates, "MRI r2 and r2 ∗ mapping accurately estimates hepatic iron concentration in transfusion-dependent thalassemia and sickle cell disease patients," *Blood*, vol. 106, no. 4, pp. 1460–1465, 2005.

[33] K. Tziomalos, V. Perifanis, Z. J. Wang, and E. Al, "Liver iron content determination by magnetic resonance imaging," *World J. Gastroenterol.*, vol. 16, no. 13, pp. 1587–1597, 2010.

[34] W. Liu and J. A. Frank, "Detection and quantification of magnetically labeled cells by cellular MRI," *Eur. J. Radiol.*, vol. 70, no. 2, pp. 258–264, 2009.

[35] K. M. Krishnan, "Biomedical nanomagnetics: A spin through possibilities in imaging, diagnostics, and therapy," *IEEE Trans. Magn.*, vol. 46, no. 7, pp. 2523–2558, Jul. 2010.

[36] M. Nahrendorf, E. Keliher, B. Marinelli, P. Waterman, P. F. Feruglio, L. Fexon, M. Pivovarov, F. K. Swirski, M. J. Pittet, C. Vinegoni, and R. Weissleder, "Hybrid PET-optical imaging using targeted probes," *Proc. Nat. Academy Sci.*, vol. 107, no. 17, pp. 7910–7915, 2010.

[37] P. R. Seevinck, J.-H. Seppenwoolde, T. C. de Wit, J. F. W. Nijsen, F. J. Beekman, A. D. van het Schip, and C. J. G. Bakker, "Factors affecting the sensitivity and detection limits of MRI, CT, and SPECT for multimodal diagnostic and therapeutic agents," *Anti-Cancer Agents Med. Chem.*, vol. 7, no. 3, pp. 317–334, 2007.

[38] A. Rahmim and H. Zaidi, "PET versus SPECT: Strengths, limitations and challenges," *Nuclear Med. Commun.*, vol. 29, no. 3, pp. 193–207, 2008.

[39] A. von Wallbrunn, C. Holtke, M. Zuhlsdorf, W. Heindel, M. Schafers, and C. Bremer, "In vivo imaging of integrin alpha v beta 3 expression using fluorescence-mediated tomography," *Eur. J. Nuclear Med. Molecular Imaging*, vol. 34, no. 5, pp. 745–54, 2007.

[40] E. E. Graves, J. Ripoll, R. Weissleder, and V. Ntziachristos, "A submillimeter resolution fluorescence molecular imaging system for small animal imaging," *Med. Phys.*, vol. 30, no. 5, pp. 901–911, 2003.

[41] T. Gambichler, G. Moussa, P. Regeniter, C. Kasseck, M. R. Hofmann, F. G. Bechara, M. Sand, P. Altmeyer, and K. Hoffmann, "Validation of optical coherence tomography in vivo using cryostat histology," *Phys. Med. Biol.*, vol. 52, no. 5, p. N75, 2007.

[42] M. Capek, R. Wegenkittl, and P. Felkel, "A fully-automatic stitching of 2D medical data sets," 2002 [Online]. Available: http://citeseerx.ist.psu.edu/viewdoc/summary?doi=10.1.1.25.5577